Discover Mechanical Engineering

Research

Hydraulic micromotor powered dissector for minimally invasive therapy

Manjeera Vinnakota[1] · **Kishan Bellur**[1] · **Sandra L. Starnes**[2] · **Mark J. Schulz**[1]

Received: 26 August 2024 / Accepted: 12 December 2024
Published online: 23 January 2025
© The Author(s) 2025 OPEN

Abstract

To address the challenges of biopsy and intratumoral drug delivery using microdevices, a miniature multifunctional tethered device that has tissue cutting, biopsy and drug delivery capabilities is presented in this paper. The cutting module in the prototype is hydraulically powered and has an outside diameter (OD) of 2 mm at the tip and a cutter attached to 500 µm drive shaft. The hydraulic micromotor prototype was fabricated using micro additive manufacturing. It was tested using a benchtop set-up and had an average speed greater than 100,000 RPM at a water flowrate of 45 mL/min and a speed of about 34,000 RPM at 15 mL/min flowrate. This micromotor design was numerically modeled using 3D-transient simulations in ANSYS CFX to determine its performance characteristics and internal resistance. Preliminary testing was performed using cutting modules with five cutter geometries on agar tissue phantoms of different concentrations and other biological materials. The dissection ability of the cutting module, its ability to deliver particles, and collect biopsy samples were successfully demonstrated. Scaling the 2 mm OD device further, a 1 mm OD micromotor, with a nominal output shaft diameter of 250 µm, was fabricated and operated with air establishing the proof of concept.

Graphical Abstract

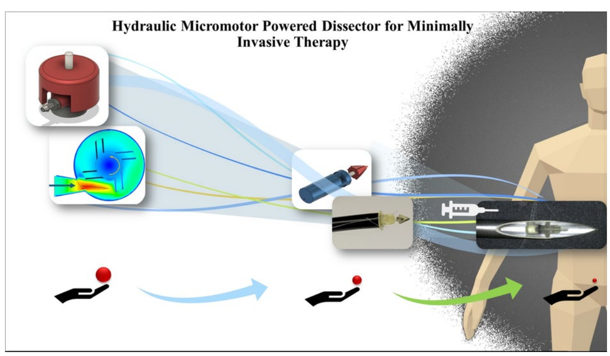

Supplementary Information The online version contains supplementary material available at https://doi.org/10.1007/s44245-024-00083-2.

✉ Manjeera Vinnakota, vinnakbm@mail.uc.edu; ✉ Mark J. Schulz, schulzmk@ucmail.uc.edu; Kishan Bellur, bellurkn@ucmail.uc.edu; Sandra L. Starnes, starnesl@ucmail.uc.edu | [1]College of Engineering and Applied Sciences, University of Cincinnati, Cincinnati, OH 45221, USA. [2]College of Medicine, University of Cincinnati, Cincinnati, OH 45221, USA.

Keywords Hydraulic micromotor · Micro additive manufacturing · Minimally invasive surgery · Hydraulic actuators · ANSYS CFX

1 Introduction

Evolution of minimally invasive procedures requires overcoming challenging barriers such as the reach of the devices. Reach is constrained by the device size, its navigation capabilities, and the ability to traverse through or around biological structures along the way. For example, a key step in procedural planning for a biopsy is the strategy to access the target depending on its location and the ability of existing instrumentation to reach the tumor. In cases where the tumor is hard to access, a surgical biopsy may be required. Increased reach and dexterity of instrumentation potentially decreases the invasiveness and provides an opportunity to develop highly targeted therapies. Improving the reach and flexibility of minimally invasive instrumentation is an active academic and commercial research area. Solutions are being developed for minimally invasive and non-invasive interventions utilizing numerous tetherless micro/nano devices [1–5], tethered devices [6, 7] and robotic systems with increased dexterity and precision [8].

Despite the advances, controlled movement of microdevices in viscoelastic media and tissue for tumor penetration or biopsy is still a challenge. Since collection of biopsy samples requires retrieving the microdevices after deployment to the desired location, complex tracking and control are required. One of the solutions proposed was to retrieve the sample collected by magnetic microrobots using a guide wire like a fishing line [9, 10]. A tethered device with a hydraulic micromotor powered cutter is presented in this paper to explore the possibility of penetrating the tumor for sample retrieval and drug delivery. A 2 mm target size is of particular interest as the needle typically used for a core needle biopsy is 2.1 to 0.91 mm OD [11]. Considering an average tumor cell diameter of 20 µm [12], the 2 mm tip would cover about 100 tumor cells.

Amount and type of drug or a biopsy sample that can be carried by a single microrobot is also severely limited, thus requiring a swarm of microrobots [13]. Even though a tether would alleviate problems such as retrieval and the amount of on-board drug, the reach is severely limited by the length and diameter of the tether. A tethered device's reach can, to some extent, be improved by reducing its diameter. However, as the size reduces the ability to perform operations such as cutting become challenging. The tethered device detailed in current work utilizes a microhydraulic motor developed by the authors to power a cutter and demonstrated dissection ability on tissue phantoms. The micromotor size is comparable to a commercial steerable cardiac catheter (~ 2 mm) so that the tendon based steering mechanism can be leveraged for navigation. Solutions combining the micro/nano devices with the commercial devices like catheters have the potential to accelerate the maturity from research lab to commercialization [6, 7, 14, 15]. Such a hybrid system combines the advantages of tetherless microrobots (reach) and tethered devices (sample retrieval, amount of drug, delivery closer to target) to advance the therapeutic options currently available.

The design and development of a miniature multifunctional tethered device that has tissue cutting, biopsy and drug delivery capabilities is presented in this paper.

2 Methods

2.1 Prototyping

The prototype device consisted of a hydraulic cutting module mounted at the distal end of a tether. The cutting module comprised of a hydraulic micromotor, cutter, and a stainless steel inlet conduit. The design details are presented below.

Micromotor and cutter fabrication: The micromotor designs presented in this paper evolved from the previous work on miniature hydraulic motors by the authors [16, 17]. It has 3 core components as in the previous scaled-up designs, i.e., cap, base and rotor, and works based on the principle of an impulse turbine. The main body of the cap has an outside diameter of 2 mm. The inlet nozzle (conical) has a mean diameter of ~ 250 µm. The rotor has 4 blades and an output shaft of 500 µm diameter. The CAD cross-section of the micromotor is shown in Fig. 1. The drum was

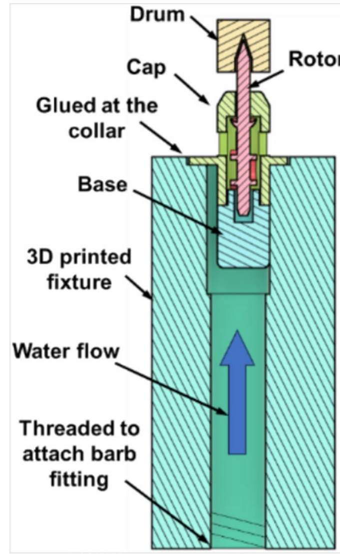

Fig. 1 CAD cross-section of micromotor prototype in a fixture. Figure not to scale to label individual components

attached in place of a cutter for RPM experiments (Sect. 2.2). A custom fixture was designed for holding the micromotor during the RPM experiments as shown in the figure. Supportless micro additive manufacturing (Projection µSLA technology) was utilized to avoid post-processing defects and improve precision of the components. BMF microArch S-140 printer (BMF, Maynard, MA, USA.) was used for manufacturing hydraulic micromotor components using HTL resin. Since the device is intended for biomedical applications, instead of the HTL resin, BMF BIO which is a medical grade resin [18] can be used for fabricating the future iterations of the device. The components were assembled using adhesive (Gorilla super glue). Medical grade glues, such as cyanoacrylate super glue from Adhesive Systems, Inc. [19], can also be used in place of the non-biocompatible glue used for the proof-of-concept. The assembled micromotors were tested with air to verify proper operation before assembling the rest of the components.

Different cutting tools were created for attaching to the micromotor output shaft: (1) re-sized piercing needle tip and (2) 3D printed cutters. A 20 g piercing needle was cut and ground such that approximately 1 to 2 mm of shank was available beyond the bevel tip for assembly (Fig. 2). The bevel tip was attached to the micromotor output shaft using adhesive. Also, cutters of 4 different baseline geometries were 3D printed in HTL resin (BMF microArch S-140 printer) and attached to the output shaft. The cutter geometries and printed porotypes are shown in Fig. 3. The intent for creating these variants was to study the relative cutting action between the prototypes using agar tissue phantoms.

Cutting module and full device fabrication: The 3D printed fixture for the RPM measurement set-up was replaced with about 2 inches of stainless steel tube (8988K19, McMaster-Carr, Elmhurst, IL, USA.). The tube forms an annular fluid channel of 143 µm (Fig. 4) around the micromotor to feed fluid into the inlet nozzle. The prototype micromotor was attached to the steel tube using adhesive. A glue bead was created around the collar and allowed to dry completely to prevent leaks. Silicone Tubing, 3/32" (2 mm) ID was used to connect a stainless steel dispensing needle (75165A265, McMaster-Carr, Elmhurst, IL, USA.) from a syringe to the steel tube of the cutting module prototype (Fig. 5). Five devices were fabricated with different cutter geometries presented in Fig. 3.

2.2 Experimental set-ups

2.2.1 RPM measurement

A single channel programmable syringe pump (NE-1010, New Era Pump Systems Inc., Farmingdale, NY, USA.) with a 60 mL syringe was used to control the water flowrate through the device. The prototype micromotor in a 3D printed fixture (Fig. 6) was held by the vibration damping clamp (3015T999; McMaster-Carr, Elmhurst, IL, USA.) and the water line from syringe pump was connected to the prototype via the fixture. The prototype was run using air to verify shaft rotation and integrity of the full assembly prior to connecting with the syringe pump. A black cylinder (drum) of 2 mm diameter and height was attached to the output shaft. The manufacturer supplied retroreflective tape (2 mm wide) was attached to the cylinder on the flat face over the full length of cylinder. A laser tachometer (LH900RF, EHDIS, Amazon, Seattle, WA,

Fig. 2 20g piercing needle tip as a cutting tool (cut and ground at red dashed line)

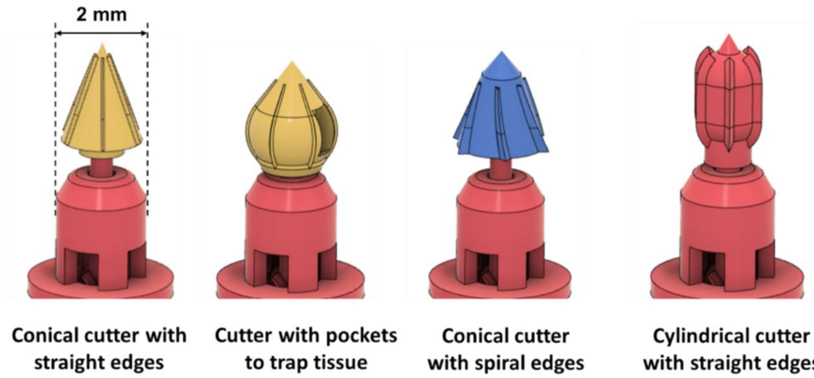

Fig. 3 CAD models of various cutter geometries

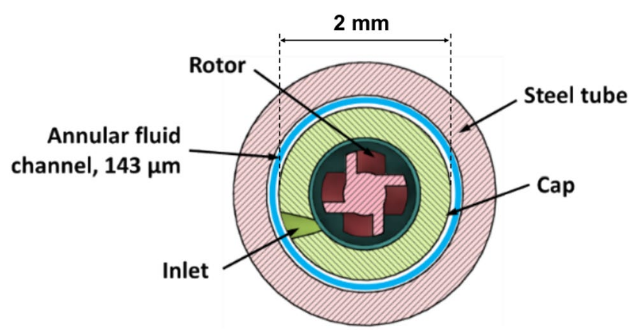

Fig. 4 Annular fluid channel (highlighted in blue) formed after assembly of steel tube

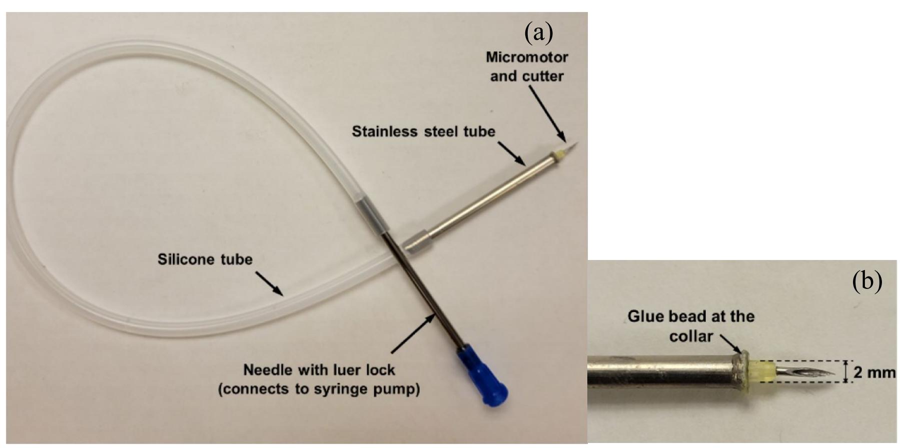

Fig. 5 (**a**) Prototype device assembly for testing with agar tissue phantoms (**b**) Glue bead to prevent leaks at the collar

USA.) was used for RPM measurement. The tachometer was mounted on a stand at 4 to 6 inches from the device with the laser perpendicular to the axis of the device as shown in Fig. 7. The data sampling rate was set to 30 Hz on the tachometer.

2.2.2 Experiments with tissue phantoms

Agar gel phantoms are commonly used by researchers to simulate the properties of different types of tissues. The limitation of gel phantoms is that they are homogeneous and do not have the morphology of biological tissue.

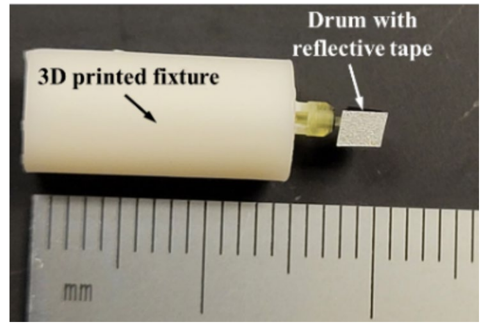

Fig. 6 Micromotor in 3D printed fixture with drum and reflective tape for RPM measurement

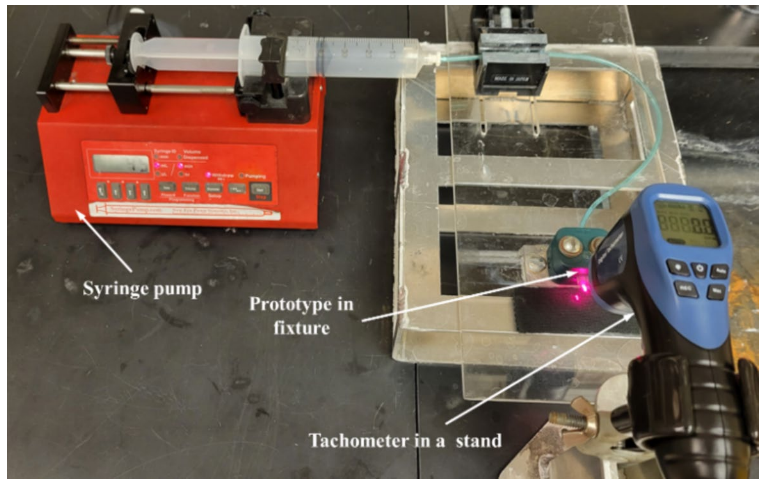

Fig. 7 Experimental set-up for RPM measurement

However, for proof of concept studies, gel phantoms work very well as they mimic some mechanical properties of interest (e.g., shear modulus) and are safe, easy to handle, store and are inexpensive compared to using actual tissue. Therefore, gel phantoms are preferred for the initial testing by many research studies. A 2 g agar gel was used for mimicking liver and breast tissue by Manickam et al. [20]. Wang et al. used 0.6%, 0.8% and 1% agar gels for demonstrating a drug delivery micro driller [21]. 0.2% agar gel was used for simulating blood clots by Jeong et al. [22]. For the current study, 0.6%, 0.8%, 1% and 2% agar gel tissue phantoms were prepared for testing the cutting action of the prototypes. 0.6% to 1% agar phantoms were shown to have shear moduli similar to the human brain [21, 23]. The 2% agar phantom is representative of a normal human breast and liver tissue [20]. The agar powder (Landor Trading Co., 900 strength, Amazon, Seattle, WA, USA.) and 5 drops of red gel food coloring (Simple Truth™ Natural Food Color Tubes, Kroger, Cincinnati, OH, USA.) were added to room temperature distilled water and stirred. The solution was boiled for 1 min and transferred to petri dishes. Once the gels were at room temperature, the petri dishes were transferred to a refrigerator for 24 h. The gel samples were brought back to room temperature before testing. For testing the prototypes on non-homogeneous materials, grapes, blueberries, and chicken liver were procured from Whole Foods Market. These samples were also brought to room temperature prior to testing.

The flowrate on the syringe pump was set to 35 mL/min. The cutter rotation was initiated prior to coming in contact with the gel by pumping 10 mL of water into the prototype. The gel specimen was placed in a petri dish and held vertically by hand so that the cutter tip is perpendicular to the specimen surface as shown in Fig. 8. The steel tube was held in hand and positioned such that the tip touches the gel specimen surface. A gentle circular motion was applied to the device to initiate cutting or enlarging the hole. If the cutter stalled, the device was pulled back and reinserted using a pecking motion. For all test cases, 40 mL of water was run through the device before stopping the syringe pump (10 mL was left in the 60 mL syringe at the end of the experiment). The hole created was imaged after removing water from the cut by gently blowing air into it. Five different cutters were tested using 4 concentrations of agar gel tissue phantoms.

Duration of the test was limited to 40 mL of water at a given flowrate to avoid refilling the syringe and running the test in multiple passes which could introduce experimental errors for a side-by-side comparison of the cutters.

Procedure for biopsy experiment: Ability to perform biopsy was one of the desired device functions. For this experiment, a cutter with pockets shown in Fig. 3 was used. An empty 60 mL syringe was operated in reverse to apply suction. Therefore, there was no fluid flow to rotate the cutter. The prototype was inserted 1.5–2 cm into the bulk of tissue phantom (~ 1 cm thick) by applying axial force on the device. Once in position, suction was applied by manually pulling the syringe plunger backward. During suction, the agar gel entered the body of micromotor through its outlet openings and was stored around the rotor in the body of the cap. The plunger on the syringe was manually pulled back 3 to 4 times (while maintaining the pull force on the plunger) before retracting the device out of the tissue phantom. The steel tube was detached from the silicone tubing and weighed by placing it in a petri dish. The mass of the retrieved prototype was compared to the mass of the empty prototype prior to the test to calculate the amount of tissue phantom retrieved by the device. The experiment was conducted with agar gels of 0.6% and 0.8% concentrations brought to room temperature. Between trials, the device was thoroughly rinsed with water and dried by forced air to remove any trapped gel. It was visually inspected after cleaning to ensure there was no gel residue. One trial was conducted without suction, during which the device was inserted to the target depth and removed 3 to 4 times and weighed.

3 Results and discussion

This section presents (1) Fabricated prototypes (2) RPM experiments results (3) Numerical modeling results (4) Tissue phantom experiments results.

3.1 Observations during prototypes fabrication

The dimensions of mating features were measured prior to assembly to ensure fit. A VHX2000 optical microscope (Keyence, Itasca, IL, USA.) was used for dimensional measurements with 3 samples. The data is shown in Table 1. No dimensional issues that would prevent assembly were detected.

Micromotor parts and assembled prototypes (no cutters) are presented in Fig. 9. 3D printed cutters in HTL resin are shown in Fig. 10a. These were assembled to the output shaft of the micromotor to function as cutting tools (shown in Fig. 10b). The cutting modules were fabricated by attaching steel tubes to the micromotors as described in Sect. 2.1 to create fluid lines to the micromotor inlet and to attach a tether. Cutting modules with different cutter geometries ready to be tested are shown in Fig. 11. The collar on the cap was sized to fit in the custom fixture for RPM testing. Since the same batch of micromotor parts (same design) were used for creating the cutting modules for testing with agar tissue phantoms, the collar protrudes slightly beyond the steel tube.

During the inspection of prototype components, it was observed that 2 types of rotors were printed. One set had the correct orientation of blades as per the CAD model and the other set had mirrored blades i.e., the inlet jet would hit the convex side of the blade instead of the concave side. Both the blade orientations are shown in Fig. 12. Experiments were conducted using micromotors assembled with both types of rotors. The experimental data is presented in Table 2.

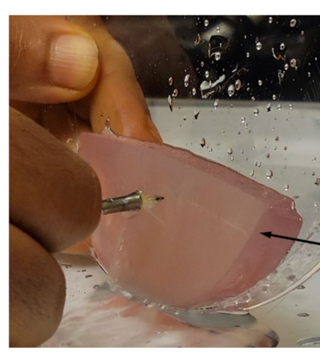

Fig. 8 The cutting module prototype and agar phantom held in place during the experiment

Table 1 Dimensional data of the components used for 2 mm OD micromotor prototypes

Feature	Description	CAD Nominal (µm)	Average (µm)
	Base bearing OD	1200	1234
	Base bearing ID	700	709
	Cap bearing ID	750	771
	Cap ID	1300	1363
	Rotor shaft OD	500	516

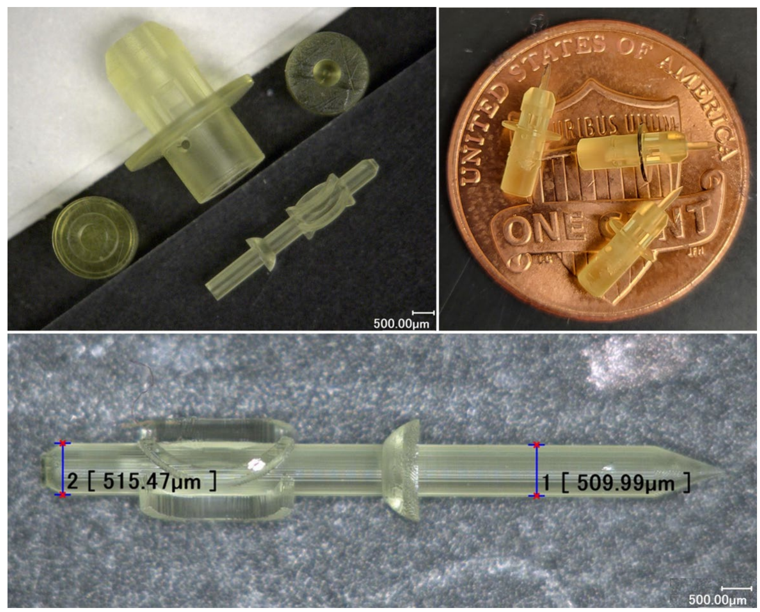

Fig. 9 Micromotor prototypes, OD 2 mm and a drive shaft of 500 µm (nominal)

To investigate the possibility of further scaling, the 2 mm OD device models were scaled down to 1 mm OD (output shaft diameter of 250 µm) and they were printed using the same BMF S-140 printer in HTL resin. No other changes were made to the design. The intent was to establish work output from the micromotor that size.

A fully assembled micromotor in a fixture is shown in Fig. 13. The operation of this micromotor using air is shown in supplementary file 1. It must be noted that the collar was sized to attach it to the larger fixture and test for output. In a tethered configuration, the collar would be more compact. The OD of the cap body was measured to be 871 µm (Fig. 14). To put this in perspective, if an average tumor cell is approximately 20 µm [12], the cutting module tip would cover about 45 cells. Circulating tumor cells can be in the range of 4 to 30 µm [24]. These can be collected from the tumor site blood/tissue sample and stored inside the micromotor body by applying suction. The outlet openings in the cap are large enough to accommodate clumps of tumor cells (275 µm × 450 µm).

3.2 RPM experiments results

The summary of data from the RPM experiments is presented in Table 2. Micromotors assembled with both the correct and mirrored rotors were tested.

During initial tests, an average RPM of 35,319 was observed with prototype 1 (correct rotor) at a flowrate of 15 mL/min and. At 25 mL/min the average RPM was 61,999. During these experiments, the prototype developed a leak at the

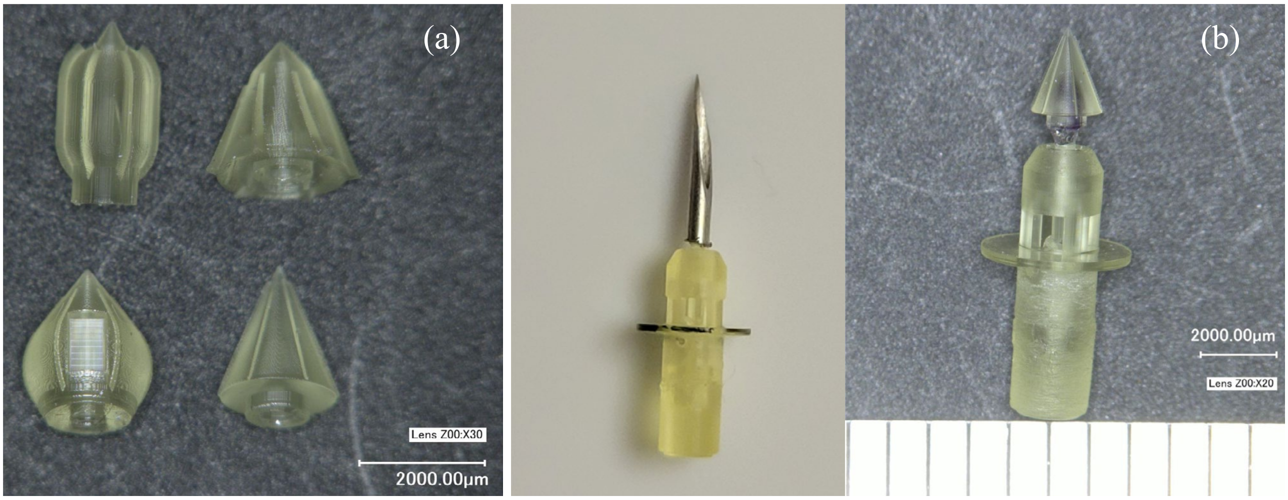

Fig. 10 (**a**) Printed cutters of different geometries to study the cutting action (**b**) Micromotors with piercing needle tip and 3D printed conical cutter as cutting tools prior to assembly with steel tubes

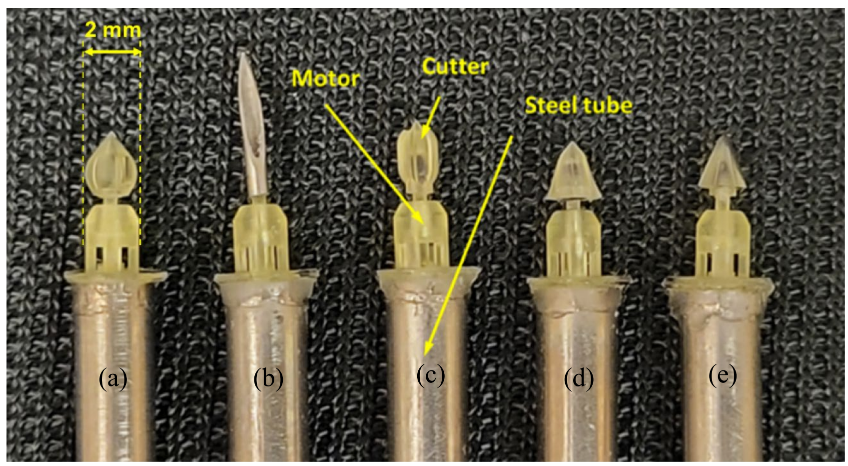

Fig. 11 Cutting modules with 5 different cutters: (**a**) Cutter with pockets to trap tissue during biopsy (**b**) Needle tip (**c**) Cylindrical cutter with straight edges (**d**) Conical cutter with spiral edges (**e**) Conical cutter with straight edges

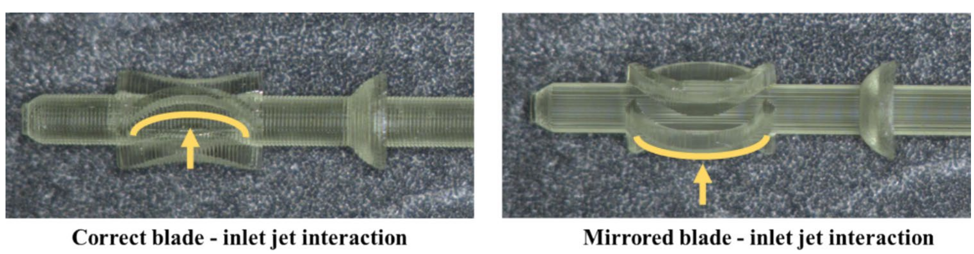

Fig. 12 Blade/inlet jet interaction in the correct and mirrored rotors

fixture-collar interface and its performance degenerated over the duration of the run. The leak was repaired using glue, and the prototype was retested. The data in Table 2 for prototype 1 was collected after attempting to fix the leak. However, a thin jet of water bypassing the device was still visible at the collar resulting in lower RPMs than prior to the detection of leak. After attempting to repair the leak on prototype for a second time, the experiment was repeated. At a flowrate of 15 mL/min, an average RPM of 34,790 was observed. At 25 mL/min, the average RPM was 63,238. These values indicate that the seal between fixture-collar improved after the second time repair.

Similarly, a leak was observed in the joint between the fixture and collar on prototypes 3 as well at higher flowrates. At lower flowrates, if a leak was present, it was harder to detect as the water exiting the device masked the water from the leak. After fixing the leak in the prototype 3, it was retested at 45 mL/min flowrate and an average RPM of 18,545 was observed.

Table 2 Experimental data collected using micromotors assembled with correct and mirrored rotors

Flowrate (mL/min)	Average RPM Prototype 1 (Correct rotor)	Average RPM Prototype 2 (Correct rotor)	Average RPM Prototype 3 (Mirrored rotor)	Average RPM Prototype 4 (Mirrored rotor)
–				
15	32,105	32,552	4792	5809
25	56,940	62,055	8203	11,010
35	75,244	91,991	11,336	15,727
45	97,328	Out of range[a]	14,261	18,956

[a]The tachometer range was 2.5 to 99,999 RPM. The RPM was greater than the maximum value of 99,999

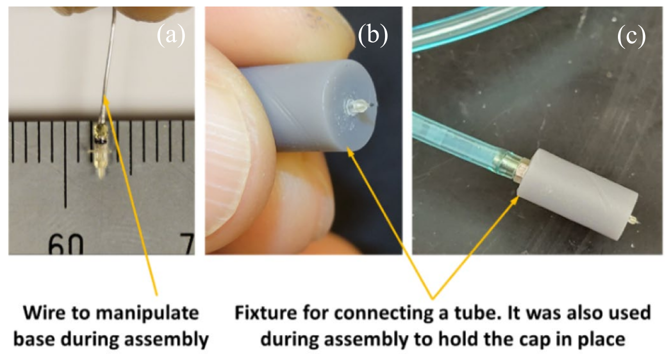

Fig. 13 (**a**) Wire attached to the base as a makeshift tool for assembly (**b**) 1 mm OD device in a printed fixture (**c**) Tube attached to the fixture

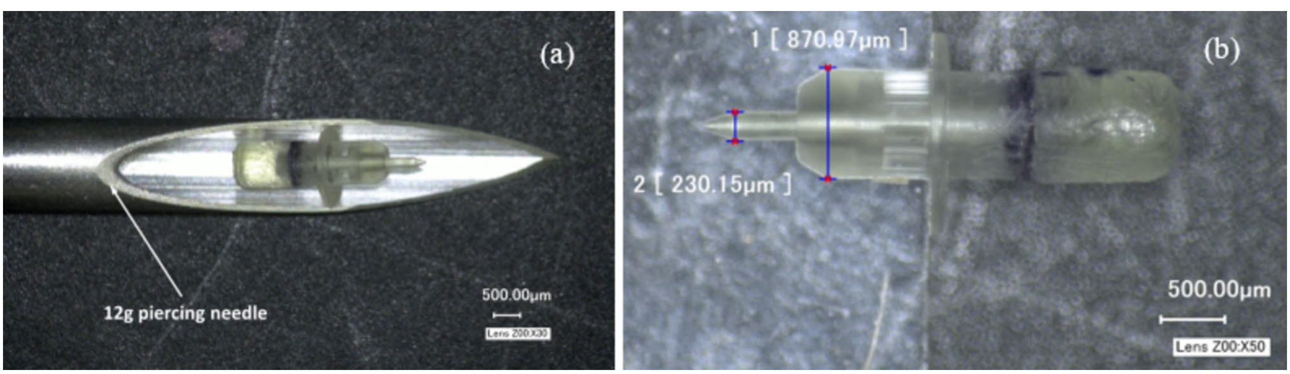

Fig. 14 (**a**) 1 mm OD micromotor in a 12g piercing needle (**b**) Micromotor tip and output shaft dimensions

Table 3 Prototype 5 RPM data. This prototype had higher internal friction due to migration of glue onto the functional surfaces

Flowrate (mL/min)	Prototype 5 Average RPM (Correct rotor)
15	7456
25	19,047
35	28,279

Prototype 5 also had multiple issues with leakage at fixture-collar interface. During the assembly or repair, glue migrated onto the micromotor functional surfaces. This increased the internal friction of the prototype. There was no rotation at 15 mL/min to start with. Rotation was initiated at 25 mL/min and then the flowrate was dropped to 15 mL/min for sustained output. The data recorded is shown in Table 3. The RPMs were much lower than the other prototypes with correct rotor.

Data was analyzed using Minitab statistical software (version 21.4.3) for generating box plots in Fig. 15 and descriptive statistics in Table 4. A larger spread was observed with higher RPM prototypes (correct rotor). This could be due to the leakage issues described earlier. At higher flowrates, the tachometer was operating at the upper end of its range (0–99,999 RPM) which could also introduce measurement error. The standard deviation calculated captures the overall spread in the experimental values whether the variation in RPM is due to inherent periodicity from spatial distribution of rotor blades or the experimental error.

The experiment was repeated in ambient light and in a dark room setting, however no significant difference in RPM readings were observed in the 2 trials conducted (Table 5). Prototype 4 at a flowrate of 25 mL/min was used for these trials.

3.3 Numerical simulations results

The modeling methodology developed in previous works [16, 17] was utilized once again for the hydraulic micromotor. The total time for the analyses was 0.05 s with a timestep of 5 µs. Based on the experiments, a mass flow inlet boundary of 0.00025 kg/s (15 mL/min) was defined. The outlets were defined as openings at atmospheric pressure. For simulation details refer to supplementary file 2, parameters are tabulated in supplementary Table 1.

A mesh independence study was conducted by varying the number of elements from 0.3 to 6 million (Fig. 16). An opposing torque of 0.1 µNm was applied to the rotor. The relative error in rotor steady state angular velocity between a mesh with 4.1 million elements and the finest mesh with 6 million elements was 0.2%. A mesh size of 4.1 million elements was used for the subsequent analyses. The change in absolute value of rotor average steady state angular velocity between these two grids was 8.6 rad/s (82 RPM). Assuming experimental data was normally distributed, ± 3 standard deviations (± 1024 RPM) would represent 99.7% of prototype 1 data, which gives a spread of 2048 RPM. The observed range in RPM from experiments was 918 for a flowrate of 15 mL/min (0.00025 kg/s) from Table 4. These values were much higher than the modeling uncertainty of 82 RPM. The assumption of normality was tested for the

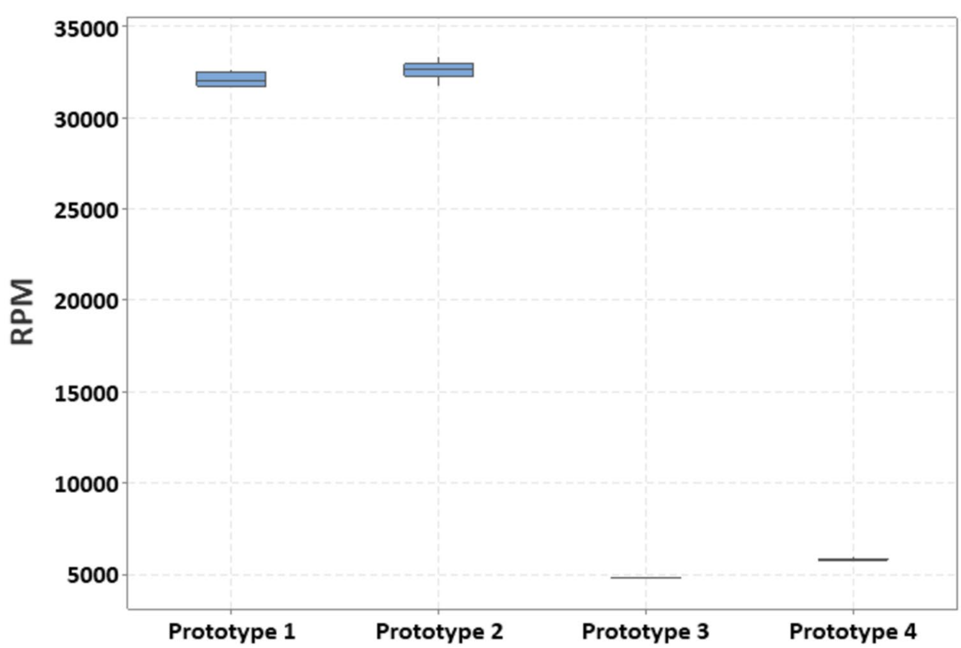

Fig. 15 Box plots of prototype micromotors output RPMs at a flowrate of 15 mL/min. Higher spread at higher RPMs was observed

Table 4 Descriptive statistics of prototype micromotor RPMs at 15 mL/min flowrate

Device	Number of Data Points	Mean RPM	Standard Deviation	Median	Range
Prototype 1	11	32,105	341.3	32,029	918
Prototype 2	17	32,552	454.8	32,608	1643
Prototype 3	21	4792	27.7	4792	100
Prototype 4	20	5809	65.9	5814	276

Table 5 Experiment with and without ambient light

Trial 1 (Average RPM)		Trial 2 (Average RPM)	
Light on	Dark	Light on	Dark
10,688.4	10,735.3	11,010.3	11,031.8

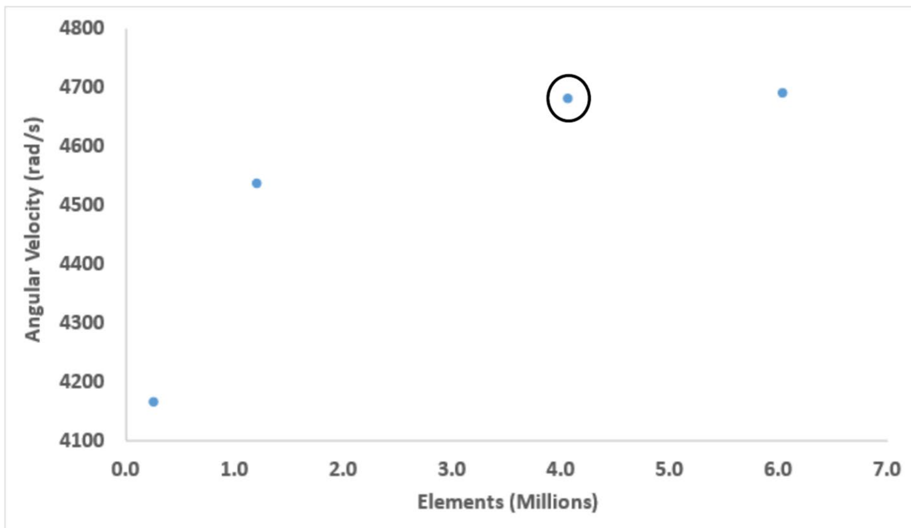

Fig. 16 Mesh independence study. A mesh with 4.1 million elements (circled) was used for subsequent analyses

experimental data of prototype 1 using Minitab statistical software and was found to be valid as the P-value, 0.321, was greater than 0.05 (for 95% confidence).

As the size of fluid domain reduces, the streamline curvature increases due to the increase in outer wall curvature. In ANSYS, to sensitize the turbulence model to the streamline curvature, modification of the turbulence production term in the form of curvature correction coefficient is available. To test the effect of this curvature correction coefficient, 4 simulations were run by varying the default value. A resistive torque of 0.25 µNm was applied on the rotor in all the cases. The inlet mass flow was set to 0.00025 kg/s. The spread in the output RPM from Table 6 (Maximum: 27,569–Minimum: 26,234 = 1335 RPM) was lower than that observed during the experiments (± 3 standard deviations, 2048 RPM for prototype 1). Therefore, for subsequent analyses, the default curvature correction coefficient with a k-ϵ turbulence model was used.

A mesh with 4.1 million elements was used to predict the performance of the model with mirrored rotor blades as well. The simulations were set up using the same boundary conditions as above, with the only difference being the rotor/inlet jet interaction. From the numerical simulations, the torque vs. RPM plot (Fig. 17) was generated for the 2 mm OD micromotors, both for the correct and mirrored rotors. Both orientations showed an inverse relationship between torque and speed as anticipated, but the mirrored prototypes generated on average 55% lower power compared to the correct orientation (Fig. 19).

The simulations assumed that there is no tilt to the rotor shaft i.e. rotor axis is along the device axis. However, during the experiments, the weight of the drum used for RPM measurement would tilt the shaft and increase the frictional resistance in the cap bearing surface. This results in a higher resistive torque or consequently lower RPM. Although the net torque could not be measured experimentally for each device, an estimate can be made from Fig. 17. For a given

Table 6 Simulation output from runs using different curvature factors

Turbulence model	Average rotor angular velocity (rad/s)	Average RPM
K-ω with curvature factor 1.25	2791.9	26,661
K-ω with curvature factor 1.1	2797.1	26,710
K-ϵ with curvature factor 1.1	2887.0	27,569
K-ϵ (default curvature factor 1)	2747.2	26,234

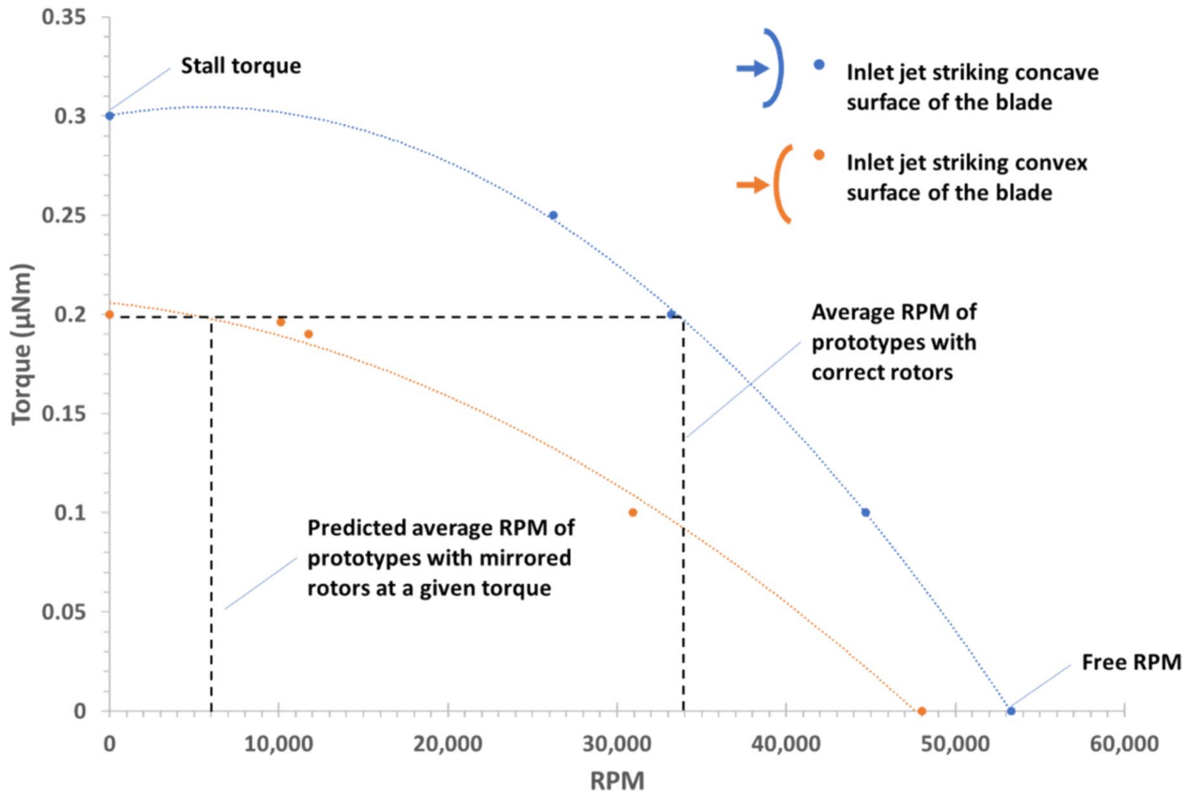

Fig. 17 Torque vs. RPM for both the correct and opposite inlet configurations. The dashed black lines indicate the predicted RPM at a given torque of 0.2 µNm for micromotors assembled with the correct and mirrored rotors

experimentally measured RPM, the corresponding torque from Fig. 17 is a combination of the internal friction due to component surface imperfections, fluid resistance and additional friction from the shaft tilt.

The endpoints of the plot (Fig. 17), i.e., stall torque point and the free RPM point represent the two extreme cases during the micromotor operation. For the free RPM case to occur, there should be no losses or frictional resistance in the system. This is an ideal case as there is always some internal resistance to the shaft rotation. On the other hand, stalling of the output shaft can happen during the micromotor operation. During the experiments stalling was observed when the resistance to cutting from the agar tissue phantoms (Sect. 3.4) was higher than the output torque of the system. In a stall situation, the fluid tries to rotate the rotor but cannot overcome the resistance on the output shaft. Therefore, the fluid pressure drops and results in a large pressure loss before the fluid exits via the outlets. The preferred operating torque of the micromotor would be in between the two extreme cases of stall and free rotation. This corresponds to the peak power zone in Fig. 19.

Prototype 1 (correct rotor) at a flowrate of 15 mL/min (0.00025 kg/s) had an average RPM of 35,319 during the experiments prior to the leak. Prototype 2 had an RPM of 32,552. Therefore, from the torque vs. RPM plot, the internal friction of the micromotor can be predicted to be ~ 0.2 µNm for an average RPM of ~ 34,000 (Prototypes 1,2). At this frictional torque, the predicted angular velocity for the devices with mirrored rotors is around 6000 RPM. Experimentally, the devices with mirrored rotors had much lower RPMs as shown in Table 2. The average RPM for prototype 3 was 4792 and prototype 4 was 5809 at 15 mL/min. These align well with the prediction of 6000 RPM from the simulations.

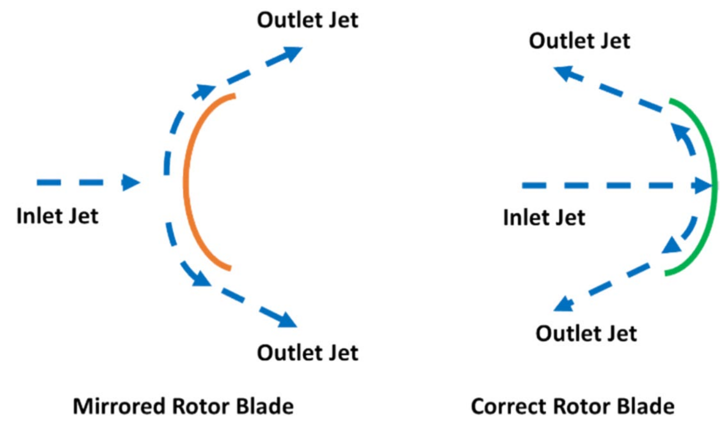

Fig. 18 Inlet jet/blade interaction in mirrored and correct rotors assuming no separation. The outlet jet is in the direction of inlet jet for the mirrored rotors reducing the amount of momentum transfer from the jet to blade, resulting in lower rotor RPMs

Although it was assumed that internal friction is the same for both the devices in the numerical model, device-to-device variation in output RPM was observed during the experiments. The frictional torque would depend on the surface finish of the components. Also, during manual assembly if any glue migrates to the surface where the rotor blades touch the base, the friction will go up due to the tackiness of the surface. This was observed during experiments with prototype 5 (Table 3).

In general, lower RPM of the mirrored devices is likely due to reduced momentum transfer between jet and blades. In the mirrored rotors, once the water jet strikes the convex surface of the blades, the outlet jet is in the direction of the inlet jet (assuming no separation) as shown in Fig. 18, therefore the amount of momentum transferred from jet to blade is reduced. The amount of jet deflection w.r.t horizontal is dependent on the blade angle and, therefore, is an important design parameter.

Performance curves from simulation data show that the peak power is 0.73 mW for the correctly assembled micromotors at 27,000 RPM and 0.33 mW at 25,000 RPM for the micromotors with mirrored rotors (Fig. 19). This is less than half of the correctly oriented rotor blades. The difference in power highlights the importance of rotor blade orientation w.r.t inlet jet, suggesting that it could be an important design parameter to optimize the torque output from the device for specific applications.

Figure 20a shows the velocity distribution on a plane passing through the inlet as the jet strikes the convex surface of the blade. The jet separates from the blade after striking it, thus reducing the momentum transfer from jet to blade. Recirculation behind the blade is also visible in Fig. 20b.

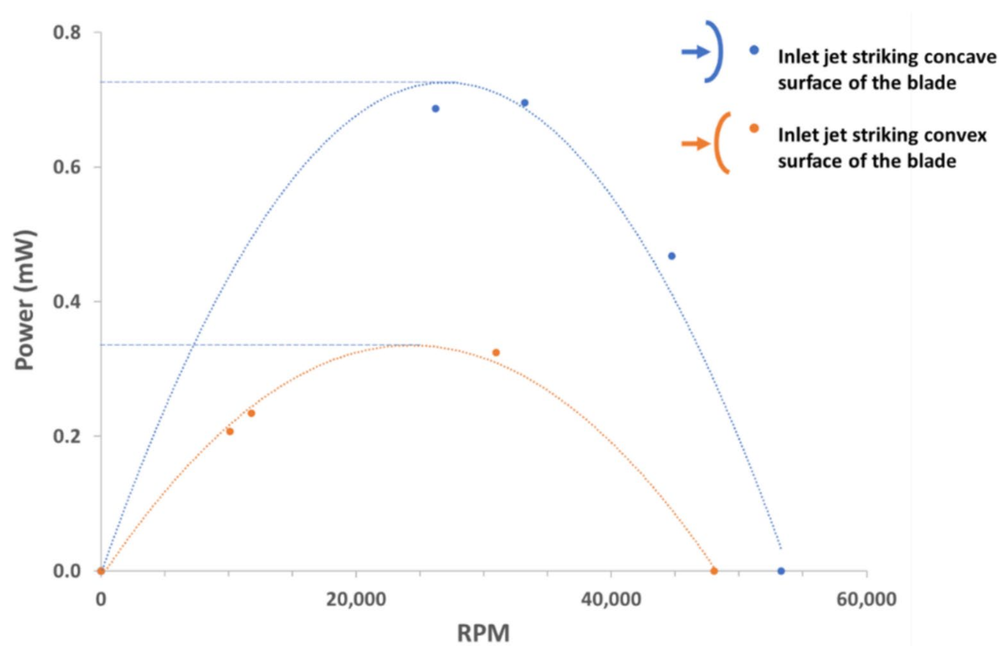

Fig. 19 Power vs. RPM for the 2 mm OD hydraulic micromotors; Both the correct and opposite inlet configurations are plotted to show the difference in peak power. Much lower peak power (less than half) in the micromotors with mirrored rotors

Figure 21a shows the theoretical interaction between correct rotor (jet on the concave surface) and the inlet water jet, it assumes that the jet is perpendicular to the blade. Whereas a tilt in the jet w.r.t the blade was observed in the simulations (Fig. 21b).

To validate the difference in power predicted by the numerical simulations (Fig. 19), an experiment was conducted with gel phantoms using prototype cutting modules with mirrored rotor and correct rotor with conical cutter (straight edges) and the needle tip cutters. The flowrate was 35 mL/min for 40 mL of water through both the cutting modules. For 2% gel, a flowrate of 45 mL/min was used. The diameter of hole (~ 4 mm) created by the cutting module with correct rotor in 1% gel phantom was much larger and well defined than the cut made with mirrored rotor cutting module. It was wide enough to accommodate the collar for the device to go through the bulk of the gel specimen (highlighted in yellow in Fig. 22a). Even with the needle tip cutter and a 2% gel phantom, the difference in cutting performance, in terms of hole diameter and depth, between the correct and mirrored prototypes was evident (Fig. 22b). The prototypes with mirrored rotors stalled frequently and did not rotate for most of the duration due to low power output. The hole created was distinctly undersized compared to the one created by the prototype with correct rotor. This difference in performance was in line with the numerical simulation results (Fig. 19), where the power of the micromotors assembled with mirrored rotors was expected to be less than half of the output when correct rotors were assembled.

3.4 Comparison with other miniature motors in an equivalent size range

In this section, the output of the hydraulic micromotor developed is compared to the motors with different working principles (Table 7). Experimentally the hydraulic micromotor exhibited much higher angular velocity than other motors in the literature.

3.5 Tissue phantom experiment results

Overall, the cutting modules demonstrated the ability to cut the agar tissue phantoms and other materials such as grapes, blueberries, and chicken liver. Delivery of particles along the cutting module travel path and the ability to collect a biopsy sample were also demonstrated. Some cutter geometries were better suited for certain agar gel concentrations. For instance, the conical cutter with straight edges performed better than the other cutters, in terms of cut diameter and depth, for concentrations of 0.6–1%, whereas the needle tip cutter performed better in the 2% agar phantom (Fig. 23). This was an important finding that emphasized the need for designing application specific cutters to achieve optimal device

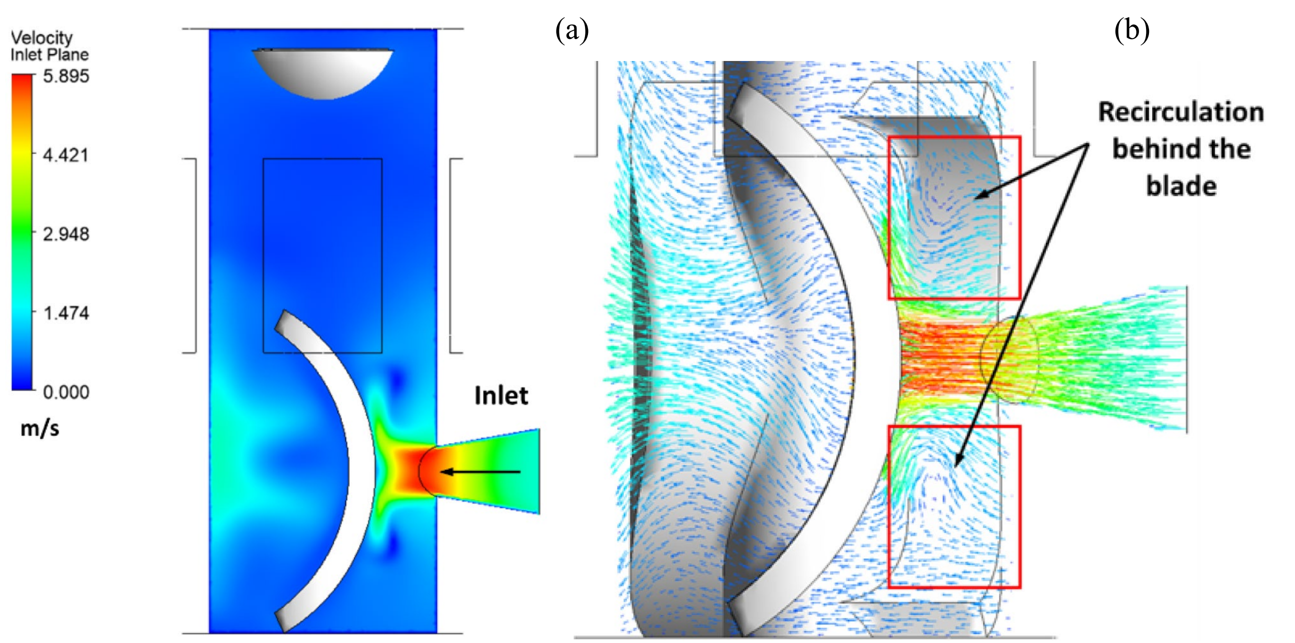

Fig. 20 (**a**) Velocity profile at the convex surface where the jet strikes the blade (**b**) Velocity vectors showing recirculation behind the blades

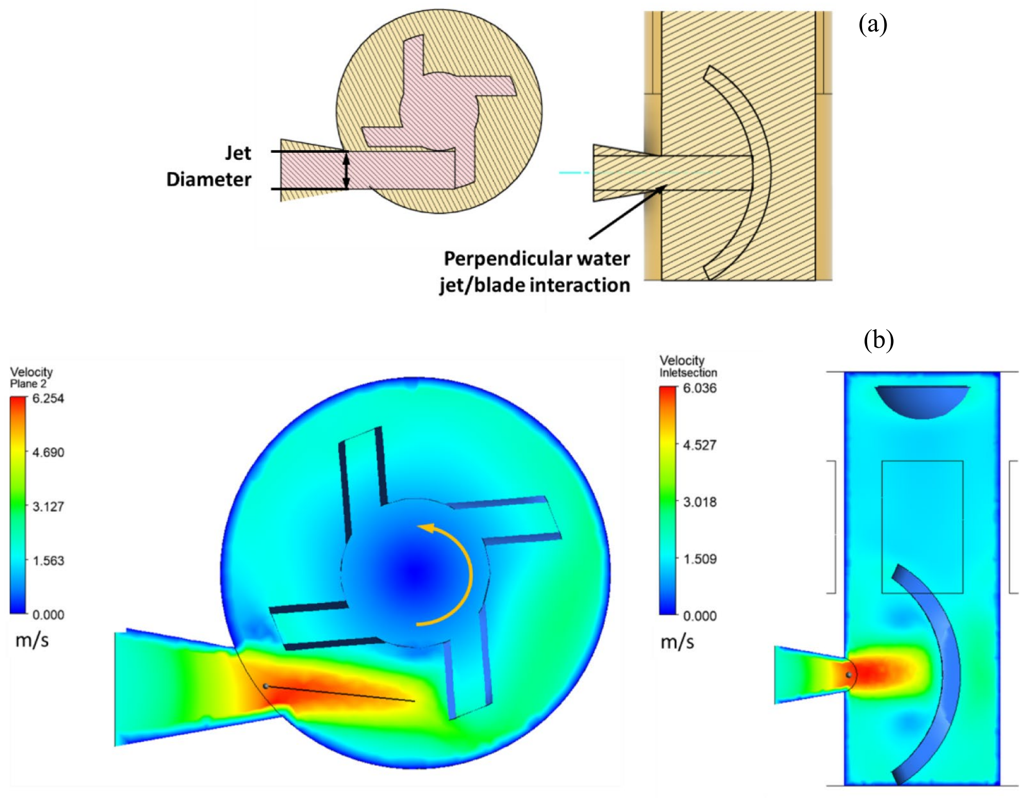

Fig. 21 Jet-blade interaction in 2 mm OD device: (**a**) Theoretical (**b**) A tilt in the jet w.r.t the blade was observed in the simulations. Orange arrow indicates the direction of rotor rotation

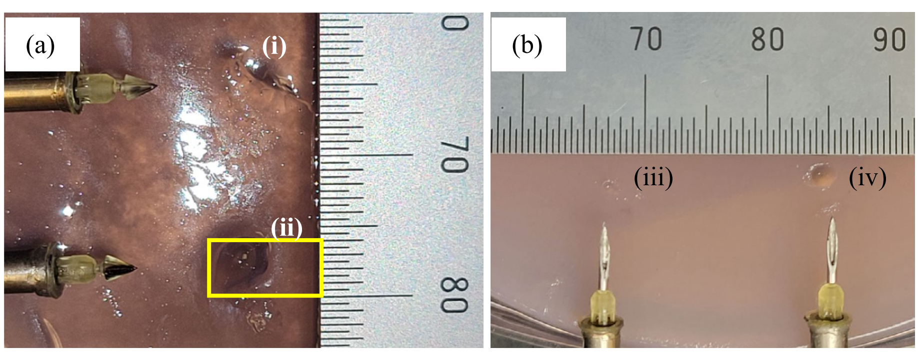

Fig. 22 (**a**) Cuts in 1% agar tissue phantom using conical cutter (straight edges) at 35 mL/min flowrate for 40 mL of water through the cutting module: (i) Mirrored rotor (ii) Correct rotor. (**b)** Cuts in 2% agar tissue phantom using needle tip cutter at 45 mL/min flowrate for 40 mL of water through the cutting module: (iii) Mirrored rotor. The cut was much smaller compared to the cut made by prototype with correct rotor in it (iv) Correct rotor

performance. In general, as the strength of the agar gel increased, the depth of cut had to be reduced to prevent the cutter from stalling. The cutting depended on the sharpness, depth of cut, torque, and angular velocity of the cutting tool.

Experiments were conducted using the needle tip cutter prototype (correct rotor) on grapes, blueberries, and chicken liver. Unlike agar phantoms, these test materials are not homogeneous and have specific morphologies. The grape was cut in half and the skin of the blueberry was peeled to expose the inside pulp to the cutter. In the case of chicken liver, the cutter was brought in contact with the smooth outer surface. A flowrate of 45 mL/min was used for pumping about 40 mL of water through the device for each run. It was observed that the performance of the needle cutter, in terms of

Table 7 Comparison of hydraulic micromotor with other miniature motors in an equivalent size range

Motor	Notes	Stall Torque (μNm)	RPM	Peak Power (mW)
Hydraulic micromotor	2 mm OD at the tip	0.3	34,000 at 15 mL/min 100,000 at 45 mL/min	0.73
Electric motor	2.4 mm OD from Orbray [25]	10	100–6000	Not reported by the manufacturer
Electro-Conjugate Fluid motor	2.8 mm OD [26]	Not reported	1200	0.2
Ultrasonic motor	2.7 mm OD ultrasonic motor with a foil type stator (Ti polymer) [27]	10.2*	2500–5300	Not reported

*Starting torque

the resultant cut, was similar to what was observed during the experiments with the 2% agar phantom. The cutter stalled when it got caught on the fibers in the grape or when the resistance to cutting was high. The cuts made in chicken liver are shown in Fig. 24a, and Fig. 24b, c are the cuts in grape and blueberry. These results are promising as they showcase the ability of the prototype to cut not just agar phantoms but also biological structures.

The heat generated during device operation is primarily frictional heat from the interaction of the cutting tool and tissue or phantoms. This heat would be dissipated by the fluid exiting the micromotor. The surrounding structures that the device is in contact with also help in heat dissipation. As a reference for assessing the heat generated by the millirobot, thermal effects of rotational atherectomy catheters were examined. During plaque removal, the mechanical cutting action between the rotating cutting tool (typically 135,000 to 180,000 RPM [28]) and arterial plaque also generates heat. Saline flows inside the catheter sheath for cooling and mixes with blood at the sheath exit. Therefore, the blood flow, along with the saline flow (flowrate of ~ 14 mL/min [29]), dissipates the heat generated during the procedure [29, 30]. The function of the fluid exiting the micromotor (flowrate of 35 mL/min was used in the tissue phantom experiments) is similar to that of the flush solution used to provide lubrication and cooling in an atherectomy catheter.

The syringe was filled with a suspension of iron particles (325 mesh ultra fine, Consolidated Chemical & Solvents Store, Amazon, Seattle, WA, USA.). 1.4 g of particles were sonicated in 100 mL of water for 1 min. The prototype cutting module was run as described earlier for creating a path using this iron particle in water suspension to deliver the particles into 0.6% agar gel specimen. The same flowrate of 35 mL/min was used to rotate the cutter as it traversed through the specimen. During the experiment, some of the particles settled in the syringe as no other solvent or surfactant was added to form a colloidal solution. Despite this settling, the iron particles were delivered along the path of prototype motion as shown in Fig. 25. Instead of the iron particle suspension, different suspensions of nanoparticles or drugs can be used for intra-tumoral delivery.

An improvement in cutting action was observed if the knife edges extend to the tip as in the conical cuter with straight edges. The spiral cutter had a nose cone with a larger angle at the tip and the cutting edges started beyond the nose cone as shown in Fig. 26. This resulted in no cutting till the cutter was pushed in by hand to a point past the nose cone for the gel phantom to come in contact with the cutting edges. The same was observed for the cylindrical cutter

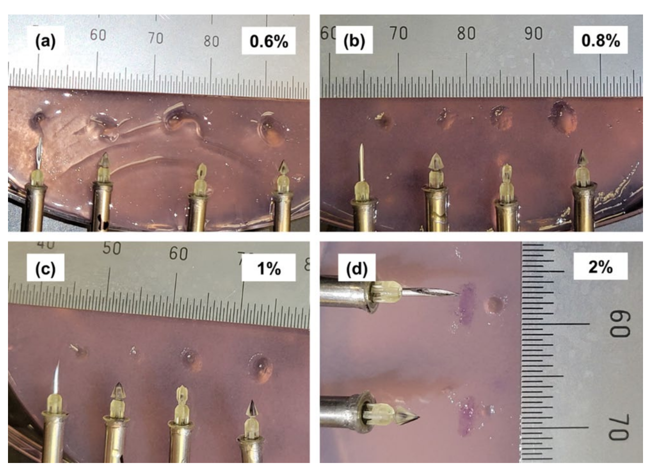

Fig. 23 Cuts in agar tissue phantoms of different concentrations using all 4 cutters at 35 mL/min flowrate for 40 mL of water through the cutting module. For 2% gel phantom 45 mL/min flowrate was used. Sequence from left to right in (**a**–**c**): Needle tip, conical cutter with spiral edges, cylindrical cutter with straight edges and conical cutter with straight edges (**d**) Needle tip (top), conical cutter with straight edges (bottom)

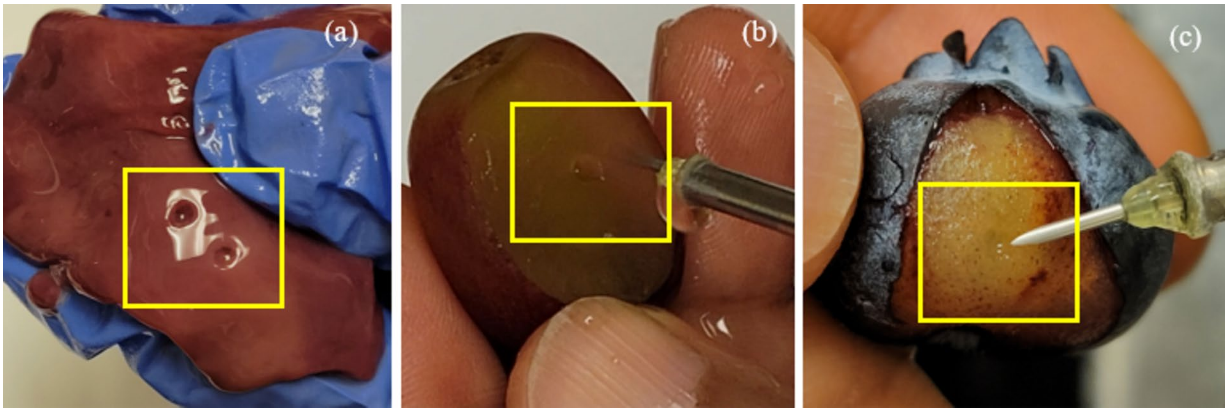

Fig. 24 Cuts during experiments using: (**a**) Chicken liver (**b**) Grape (**c**) Cut initiated in a blueberry. In all the cases, cuts could be made using the needle tip cutter prototype

with straight edges as well. The base diameter of the spiral cutter (2 mm) was also larger than that of the conical cutter (1.8 mm) i.e., the cone angle was larger. Overall, smaller cone angle with the conical cutter (straight edges) resulted in better cutting performance.

Biopsy experiment results: Fig. 27 shows the cutting module before and after the biopsy trial. As the concentration of gel increased, higher suction was needed to pull the sample into the device. When the pull force was removed, the plunger tended to spring back. The force required to pull the plunger back was noticeably different between 0.6 and 0.8% gels. Very little tissue (3 mg with 0.8% gel) could be sampled without suction. Mass of the collected specimen was converted to volume using the density of agar gel (average gel density of 1.1 mg/mm^3).

In the guidelines for liver biopsy, a minimum of 20 mm length sample using a 16 g needle was recommended [31]. Considering an ID of 1.194 mm for a 16 g needle, the volume of sample can be calculated to be 22 mm^3. From Table 8, most of the samples collected were much greater than this value except for one trial with 0.8% agar gel. As the gel stiffness increases, more suction is needed to collect the sample. Another unknown is how similar the stiffness of the agar gels created is to the actual liver tissue being biopsied. However, this calculation gives a good initial estimate about the prototype's ability to collect a biopsy sample.

4 Conclusions

Innovative minimally invasive instrumentation need to be dexterous and multifunctional to address the issue of reach. Microdevices being developed to improve reach have challenges in the context of biopsy and intratumoral drug delivery due to their limited ability to carry the collected sample/drug and move in viscoelastic media and tissue. Retrieval of microdevices carrying the biopsy sample is also a herculean design challenge. The miniature tethered device of OD ~ 2 mm presented herein offers a solution to the above mentioned challenges such as cutting, sample retrieval etc. The prototype device size is in the range of needles used for core needle biopsy and typical steerable

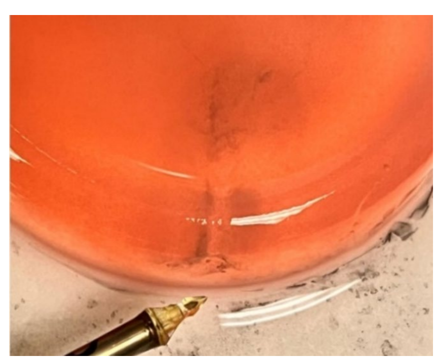

Fig. 25 Iron particles (darker coloration circled in yellow) delivered along the path of prototype as it traversed through 0.6% agar tissue phantom

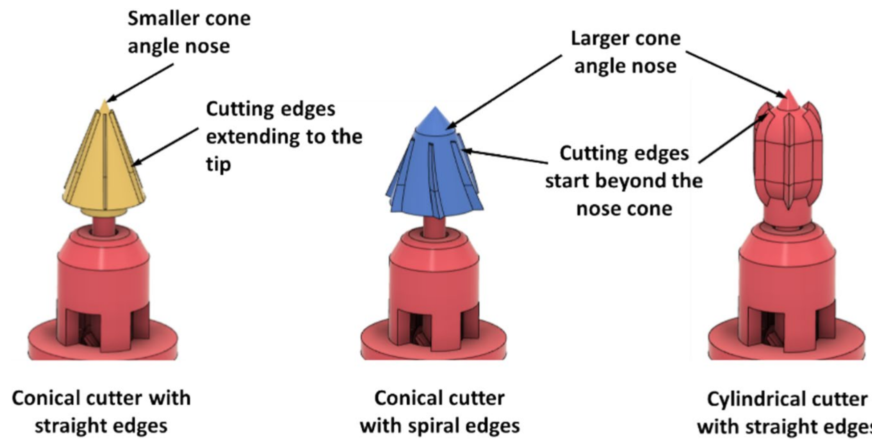

Fig. 26 Differences in geometry leading to poor performance of the cutter with spiral edges and the cylindrical cutter. Since the nose does not have any sharp edges, no cutting takes place till the depth of insertion is beyond the extent of nose cone. Cutting edges extending to the tip and a smaller cone angle are desirable

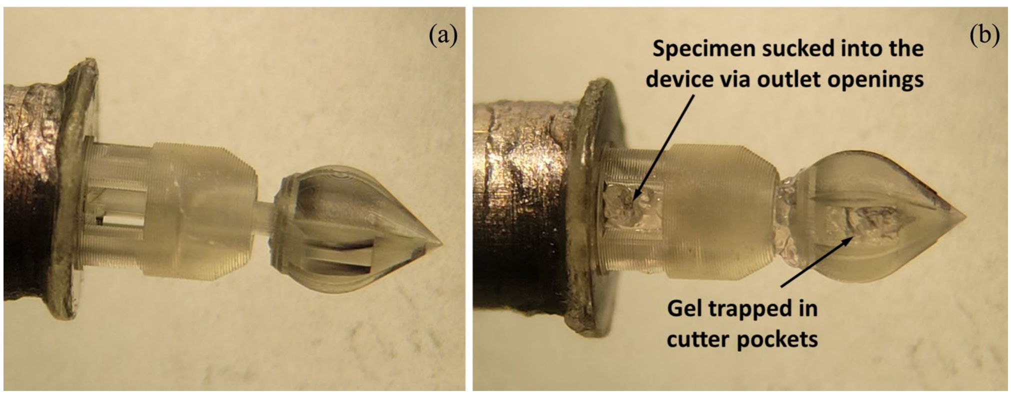

Fig. 27 (**a**) Device before biopsy experiment; (**b**) Agar tissue phantom sample collected inside the prototype after the experiment

Table 8 Tissue phantom samples retrieved using the prototype with biopsy tip

Trial	0.6% agar gel sample retrieved (mg)	0.6% agar gel sample volume (mm^3)	0.8% agar gel sample retrieved (mg)	0.8% agar gel sample volume (mm^3)
1.	70.5	64.0	36.2	32.9
2.	46.0	41.8	20.1	18.3
3.	42.9	39.0	39.3	35.7

cardiac catheters. It established a proof of concept for consistent mechanical work for tissue dissection from a hydraulic micromotor combined with other functionalities such as biopsy and particle delivery.

Hydraulic micromotors of ~ 2 mm OD (500 µm output shaft) were successfully manufactured with components printed using Projection µSLA technology. The micromotors were tested extensively using a benchtop set-up design with a syringe pump. Rotational speeds of 34,000 RPM (average) at 15 mL/min and greater than 100,000 RPM were observed at 45 mL/min water flowrate. The peak power for the 2 mm OD micromotor was estimated to be 0.73 mW at 27,000 RPM with a free RPM of 53,300 for a flowrate of 15 mL/min (0.25 mL/s). The stall torque was predicted to be 0.3 µNm. From the simulations, it was found that the peak power decreased by more than half when the inlet jet strikes the convex side of blades instead of the concave side. This degradation in performance was also observed experimentally during the RPM and tissue phantom experiments.

Cutting modules were fabricated by assembling cutters of five different geometries and fluid lines to the 2 mm OD micromotors. Tissue phantoms of different concentration agar gels (0.6%, 0.8%, 1% and 2%) to emulate human brain, breast and liver tissues were created to demonstrate the cutting module's performance. Prototypes were also successfully tested on other materials such as chicken liver, grapes etc. Of all the geometries of cutters that were tested, the conical cutter with straight edges had the best relative performance in terms of cut diameter and depth on 0.6%, 0.8% and 1% phantoms. For the 2% phantom, the needle tip cutter had a better performance. Even with as-printed polymer cutters and preliminary micromotor design, the prototypes demonstrated dissection capability on tissue phantoms and other materials such as chicken liver. These experiments highlighted the importance of optimizing the torque output of the micromotor and the cutter geometry for a specific application.

Delivery of iron particles along the path of travel of the cutting module was also demonstrated using 0.6% phantom. This is important from an intra-tumoral drug delivery perspective as a nanoparticle suspension or drug solution can be used to drive the micromotor and deliver the nanoparticles along the cutting path. A biopsy experiment was successfully conducted on 0.6% and 0.8% phantoms to demonstrate retrieval of sufficient specimen by the cutting module for histological analysis.

Scaling the 2 mm OD device further, a proof of concept 1 mm OD micromotor, with a nominal output shaft diameter of 250 μm, was fabricated and successfully operated with air. A utility patent application was filed with the United States Patent and Trademark Office (USPTO) by the University of Cincinnati Office of Innovation (reference number: U.S. Serial No. 18/756,618, Filed June 27, 2024).

Acknowledgements We thank the Institute for Electronics and Nanotechnology (IEN), Georgia Institute of Technology, Boston Micro Fabrication (BMF), 1819 Innovation Hub and the Digital Fabrication Lab at the University of Cincinnati for their support during prototyping.

Author contributions Conceptualization, methodology: M.V., M.J.S., K.B. and S.L.S.; validation: M.V., K.B. and M.J.S.; formal analysis, investigation, data curation, writing-original draft preparation: M.V. and K.B.; writing-review and editing: M.V., K.B., M.J.S. and S.L.S.; visualization: M.V.; supervision: M.J.S. and K.B. All authors have read and agreed to the published version of the manuscript.

Funding This research received no external funding.

Data availability The data presented in this study are available on request from the corresponding author. All the data are not publicly available due to the utility patent being processed (reference number: U.S. Serial No. 18/756,618, Filed June 27, 2024).

Code availability Not applicable.

Declarations

Competing interests The authors declare no competing interests.

Open Access This article is licensed under a Creative Commons Attribution-NonCommercial-NoDerivatives 4.0 International License, which permits any non-commercial use, sharing, distribution and reproduction in any medium or format, as long as you give appropriate credit to the original author(s) and the source, provide a link to the Creative Commons licence, and indicate if you modified the licensed material. You do not have permission under this licence to share adapted material derived from this article or parts of it. The images or other third party material in this article are included in the article's Creative Commons licence, unless indicated otherwise in a credit line to the material. If material is not included in the article's Creative Commons licence and your intended use is not permitted by statutory regulation or exceeds the permitted use, you will need to obtain permission directly from the copyright holder. To view a copy of this licence, visit http://creativecommons.org/licenses/by-nc-nd/4.0/.

References

1. Lee JG, Raj RR, Day NB, Shields CWI. Microrobots for biomedicine: unsolved challenges and opportunities for translation. ACS Nano. 2023;17:14196–204. https://doi.org/10.1021/acsnano.3c03723.
2. Nauber R, Goudu SR, Goeckenjan M, Bornhäuser M, Ribeiro C, Medina-Sánchez M. Medical microrobots in reproductive medicine from the bench to the clinic. Nat Commun. 2023;14:728. https://doi.org/10.1038/s41467-023-36215-7.
3. Rastmanesh A, Yaraki MT, Wu J, Wang Z, Ghoderao P, Gao Y, Tan YN. Bioinspired micro/nanomotors towards a self-propelled noninvasive diagnosis and treatment of cancer. Mol Syst Des Eng. 2021;6:566–93. https://doi.org/10.1039/D1ME00065A.
4. Schmidt CK, Medina-Sánchez M, Edmondson RJ, Schmidt OG. Engineering microrobots for targeted cancer therapies from a medical perspective. Nat Commun. 2020;11:5618. https://doi.org/10.1038/s41467-020-19322-7.
5. Wang Y, Shen J, Handschuh-Wang S, Qiu M, Du S, Wang B. Microrobots for targeted delivery and therapy in digestive system. ACS Nano. 2023;17:27–50. https://doi.org/10.1021/acsnano.2c04716.
6. Yang Z, Yang L, Zhang M, Xia N, Zhang L. Ultrasound-guided wired magnetic microrobot with active steering and ejectable tip. IEEE Trans Ind Electron. 2023;70:614–23. https://doi.org/10.1109/TIE.2022.3153809.
7. Sikorski J, Heunis CM, Obeid R, Venkiteswaran VK, Misra S. A flexible catheter system for ultrasound-guided magnetic projectile delivery. IEEE Trans Robot. 2022;38:1959–72. https://doi.org/10.1109/TRO.2021.3123865.
8. Williamson T, Song S-E. Robotic surgery techniques to improve traditional laparoscopy. JSLS. 2022;26:e2022.00002. https://doi.org/10.4293/JSLS.2022.00002.

9. Breger JC, Yoon C, Xiao R, Kwag HR, Wang MO, Fisher JP, Nguyen TD, Gracias DH. Self-folding thermo-magnetically responsive soft microgrippers. ACS Appl Mater Interfaces. 2015;7:3398–405. https://doi.org/10.1021/am508621s.
10. Gultepe E, Randhawa JS, Kadam S, Yamanaka S, Selaru FM, Shin EJ, Kalloo AN, Gracias DH. Biopsy with thermally-responsive untethered microtools. Adv Mater. 2013;25:514–9. https://doi.org/10.1002/adma.201203348.
11. VanderLaan PA. Fine-needle aspiration and core needle biopsy: an update on 2 common minimally invasive tissue sampling modalities. Cancer Cytopathol. 2016;124:862–70. https://doi.org/10.1002/cncy.21742.
12. Moore GE, Sandberg AA, Watne AL. The comparative size and structure of tumor cells and clumps in the blood, bone marrow, and tumor imprints. Cancer. 1960;13:111–7. https://doi.org/10.1002/1097-0142(196001/02)13:1%3c111::AID-CNCR2820130121%3e3.0.CO;2-Y.
13. Wang Q, Zhang L. External power-driven microrobotic swarm: from fundamental understanding to imaging-guided delivery. ACS Nano. 2021;15:149–74. https://doi.org/10.1021/acsnano.0c07753.
14. Iacovacci V, Ricotti L, Sinibaldi E, Signore G, Vistoli F, Menciassi A. An intravascular magnetic catheter enables the retrieval of nanoagents from the bloodstream. Advanced Science. 2018;5:1800807. https://doi.org/10.1002/advs.201800807.
15. Soto F, Chrostowski R. Frontiers of medical micro/nanorobotics: in vivo applications and commercialization perspectives toward clinical uses. Front Bioengineer Biotechnol. 2018;6:170.
16. Vinnakota M, Bellur K, Starnes SL, Schulz MJ. Design and modeling of a miniature hydraulic motor for powering a cutting tool for minimally invasive procedures. Micromachines. 2023;14:1338. https://doi.org/10.3390/mi14071338.
17. Vinnakota M, Bellur K, Starnes SL, Schulz MJ. Scaling a hydraulic motor for minimally invasive medical devices. Micromachines. 2024;15:131. https://doi.org/10.3390/mi15010131.
18. Materials V2 https://bmf3d.com/micro-3d-printing-materials/ Accessed 16 Oct 2024.
19. ASI MG Series medical grade cyanoacrylate super glue https://www.gluegun.com/products/asi-mg-series-medical-grade-super-glue Accessed 17 Jan 2024.
20. Manickam K, Machireddy RR, Seshadri S. Characterization of biomechanical properties of agar based tissue mimicking phantoms for ultrasound stiffness imaging techniques. J Mech Behav Biomed Mater. 2014;35:132–43. https://doi.org/10.1016/j.jmbbm.2014.03.017.
21. Wang T, Yang D, Chen J, Chow J, Hu Y, Hoang K, Ansari A. A tetherless microdriller for maneuverability and on-board cargo delivery inside viscoelastic media. In proceedings of the 2022 international conference on manipulation, automation and robotics at small scales (MARSS); IEEE: Toronto, ON, Canada. 2022; pp. 1–6.
22. Jeong S, Choi H, Cha K, Li J, Park J, Park S. Enhanced locomotive and drilling microrobot using precessional and gradient magnetic field. Sens Actuators A. 2011;171:429–35. https://doi.org/10.1016/j.sna.2011.08.020.
23. Hamhaber U, Sack I, Papazoglou S, Rump J, Klatt D, Braun J. Three-dimensional analysis of shear wave propagation observed by *in vivo* magnetic resonance elastography of the brain. Acta Biomater. 2007;3:127–37. https://doi.org/10.1016/j.actbio.2006.08.007.
24. Allard WJ, Matera J, Miller MC, Repollet M, Connelly MC, Rao C, Tibbe AGJ, Uhr JW, Terstappen LWMM. Tumor cells circulate in the peripheral blood of all major carcinomas but not in healthy subjects or patients with nonmalignant diseases. Clin Cancer Res. 2004;10:6897–904. https://doi.org/10.1158/1078-0432.CCR-04-0378.
25. Micro Motor–Japan | Orbray Co., Ltd. https://orbray.com/en/product/dccorelessmotor/supermicromotor.html Accessed 19 Jan 2024.
26. Yokota S, Edamura K. New construction of an electro-conjugate fluid-jet-driven micromotor with an inner diameter of 2 Mm. Proceed Institut Mechan Eng Part I J Syst Control Eng. 2006;220:251–6. https://doi.org/10.1243/09596518I01404.
27. Furukawa Y, Kaga T, Makita K, Wada T, Nakajima A. Development of ultrasonic micro motor with a coil type stator. In next-generation actuators leading breakthroughs; Higuchi T, Suzumori K, Tadokoro S, Eds.; Springer: London, 2010; pp. 387–399 ISBN 978-1-84882-991-6.
28. Barbato E, Carrié D, Dardas P, Fajadet J, Gaul G, Haude M, Khashaba A, Koch K, Meyer-Gessner M, Palazuelos J, et al. European expert consensus on rotational atherectomy https://eurointervention.pcronline.com/article/european-expert-consensus-on-rotational-atherectomy Accessed 10 May 2024.
29. Liu Y, Liu Y, Zheng Y, Li B, Shih A. Catheter thermal energy generation and temperature in rotational atherectomy. Med Eng Phys. 2019;70:29–38. https://doi.org/10.1016/j.medengphy.2019.06.014.
30. Sharma SK, Tomey MI, Teirstein PS, Kini AS, Reitman AB, Lee AC, Généreux P, Chambers JW, Grines CL, Himmelstein SI, et al. North american expert review of rotational atherectomy. Circulat Cardiovasc Intervent. 2019;12:e007448. https://doi.org/10.1161/CIRCINTERVENTIONS.118.007448.
31. Neuberger J, Patel J, Caldwell H, Davies S, Hebditch V, Hollywood C, Hubscher S, Karkhanis S, Lester W, Roslund N, et al. Guidelines on the use of liver biopsy in clinical practice from the british society of gastroenterology, the royal college of radiologists and the royal college of pathology. Gut. 2020;69:1382–403. https://doi.org/10.1136/gutjnl-2020-321299.

Publisher's Note Springer Nature remains neutral with regard to jurisdictional claims in published maps and institutional affiliations.